Comparison of ^{120}Sn(^{6}He,^{6}He)^{120}Sn and ^{120}Sn(α,α)^{120}Sn elastic scattering and signatures of the ^{6}He neutron halo in the optical potential

P. Mohr,[1,2] P. N. de Faria,[3] R. Lichtenthäler,[3] K. C. C. Pires,[3] V. Guimarães,[3] A. Lépine-Szily,[3]
D. R. Mendes, Jr.,[3] A. Arazi,[4] A. Barioni,[3] V. Morcelle,[3] and M. C. Morais[3]

[1]*Strahlentherapie, Diakonie-Klinikum, D-74523 Schwäbisch Hall, Germany*
[2]*Institute of Nuclear Research (ATOMKI), H-4001 Debrecen, Hungary*
[3]*Instituto de Fisica-Universidade de São Paulo, C.P. 66318, 05389-970 São Paulo, Brazil*
[4]*Laboratorio Tandar, Departamento de Fisica, Comisión Nacional de Energía*

Cross sections of ^{120}Sn(α,α)^{120}Sn elastic scattering have been extracted from the α-particle-beam contamination of a recent ^{120}Sn(^{6}He,^{6}He)^{120}Sn experiment. Both reactions are analyzed using systematic double-folding potentials in the real part and smoothly varying Woods-Saxon potentials in the imaginary part. The potential extracted from the ^{120}Sn(^{6}He,^{6}He)^{120}Sn data may be used as the basis for the construction of a simple global ^{6}He optical potential. The comparison of the ^{6}He and α data shows that the halo nature of the ^{6}He nucleus leads to a clear signature in the reflexion coefficients η_L: The relevant angular momenta L with $\eta_L \gg 0$ and $\eta_L \ll 1$ are shifted to larger L with a broader distribution. This signature is not present in the α-scattering data and can thus be used as a new criterion for the definition of a halo nucleus.

I. INTRODUCTION

In the past decade a series of experiments has been performed on elastic scattering of unstable nuclei at energies around the Coulomb barrier. It has been found that the scattering cross sections show a significantly different behavior for weakly bound projectiles compared to tightly bound projectiles such as the α particle. The small binding energy of valence nucleons in orbitals with small angular momentum leads to wave functions that extend to very large radii, exceeding by far the usual $A^{1/3}$ radius dependence. Owing to the corresponding long-range absorption, the Fresnel diffraction peak in the elastic scattering angular distribution is damped and the elastic scattering cross section at backward angles is relatively small. As a consequence, the derived total reaction cross section σ_{reac} for these exotic nuclei (e.g., ^{6}He) is much larger than for tightly bound projectile (e.g., α particle)-induced reactions. Fusion, breakup, and transfer reactions have been studied as the relevant reaction mechanisms.

As one focus on elastic scattering experiments with ^{6}He, results have been reported for heavy target nuclei such as ^{197}Au, ^{208}Pb, and ^{209}Bi [1–7] and intermediate-mass nuclei such as ^{64}Zn and ^{65}Cu [8–10]. Some data are also available for lighter target nuclei such as ^{12}C (e.g., Refs. [11,12]). In addition, elastic scattering of ^{11}Be has been studied recently [13–15]. For a complete list of references, see the recent reviews [16,17].

Moreover, a series of theoretical investigations [18–30] on ^{6}He elastic scattering has been performed in the past years; they are also summarized in the review articles by Keeley and co-workers [16,17]. The present study reanalyzes recently published data of the ^{120}Sn(^{6}He,^{6}He)^{120}Sn elastic scattering cross section [31] that filled the gap between targets with $A \ll 100$ and $A \approx 200$. We compare these results to ^{120}Sn(α,α)^{120}Sn elastic-scattering data that have been obtained in the same experiment. The similarities and differences of the weakly bound projectile ^{6}He and the tightly bound projectile α are nicely visible in this comparison.

The present study uses double-folding potentials for the real part of the potential; this type of potential is widely used in literature. The imaginary part is parametrized by Woods-Saxon potentials. The parameters of the potentials are restricted by the systematics of volume integrals that was found for many α-nucleus systems [32]; this systematics was successfully extended to ^{6}He in Refs. [4,18]. Further information on the ^{120}Sn-α potential is obtained from the analysis of angular distributions at higher energies [33–36] and excitation functions at lower energies [37,38].

The most important quantity for the description of elastic scattering data below and around the Coulomb barrier are the reflexion coefficients η_L, which define the total reaction cross section. There is a characteristic increase of the η_L from $\eta_L \approx 0$ (i.e., almost complete absorption) for small angular momenta L to $\eta_L \approx 1$ (i.e., no absorption) for large L corresponding to large impact parameters in a classical picture. It will be shown that the dependence of η_L on the angular momentum L differs significantly for ^{120}Sn(^{6}He,^{6}He)^{120}Sn and ^{120}Sn(α,α)^{120}Sn elastic scattering. This difference can be considered as a new criterion for unusual strong absorption because of the halo nature of ^{6}He.

This article is organized as follows: In Sec. II we repeat very briefly a discussion of the experimental setup that is identical to that used in Ref. [31]. Section III contains an optical-model (OM) analysis of the ^{120}Sn(^{6}He,^{6}He)^{120}Sn (Sec. III A) and ^{120}Sn(α,α)^{120}Sn (Sec. III B) scattering data and a discussion of the results (Sec. III C). Finally, conclusions are drawn in Sec. IV. Energies are given in the center-of-mass (c.m.) system except when explicitly noted as laboratory energy E_{lab}.

II. EXPERIMENTAL TECHNIQUE

The scattering experiment has been performed at the 8UD São Paulo Pelletron Laboratory at the Radioactive Ion Beams

in Brazil facility [39]. A primary ^{7}Li^{3+} beam with energies around 25 MeV and a beam current of 300 nAe hits the primary ^{9}Be target. The reaction products are collimated and enter a solenoid that focuses the primary ^{7}Li particles onto a "lollipop," where the ^{7}Li particles are stopped. Because of the different magnetic rigidity, the secondary ^{6}He and α particles do not hit the lollipop, but reach the secondary ^{120}Sn target. Typical beam intensities are about 10^4–10^5 particles per second at the secondary target position. A 3.8 mg/cm^2 isotopically enriched (98.29%) ^{120}Sn target and a 3.0 mg/cm^2 ^{197}Au target have been used as secondary targets. Because the scattering ^{4}He + ^{197}Au is pure Rutherford at forward angles in the energies of the present experiment, runs with gold targets have been performed just before and after every ^{120}Sn run to normalize the ^{4}He + ^{120}Sn cross sections [31].

The scattered particles are detected and identified in a system of ΔE and E silicon detectors. A schematic view of the setup is given in Fig. 1 of Ref. [31].

The ^{6}He beam is produced by one-proton removal from ^{7}Li in the ^{9}Be(^{7}Li,^{6}He)^{10}B reaction. However, the reaction ^{9}Be(^{7}Li,α)^{12}B may also occur in the primary target, leading to an α contamination of the secondary beam. Because of the much larger Q value of the α-producing reaction ($Q_\alpha =$ +10.5 MeV compared to $Q_{^6\text{He}} = -3.4$ MeV), the α particles have slightly higher energies around 30 MeV. The α beam contamination is clearly visible in the $\Delta E - E$ spectra in Fig. 2 of Ref. [31]. This contamination can be used to measure the ^{120}Sn(α,α)^{120}Sn elastic scattering cross section simultaneously with the ^{120}Sn(^{6}He,^{6}He)^{120}Sn experiment.

The result of the previous ^{120}Sn(^{6}He,^{6}He)^{120}Sn experiment [31] is shown in Fig. 1 together with the original analysis of Ref. [31] and the new analysis, which is discussed in the following Sec. III A. The new ^{120}Sn(α,α)^{120}Sn elastic scattering data are shown in Fig. 2 together with the theoretical results of this work. Except for the 20-MeV data that were obtained in a previous ^{8}Li + ^{120}Sn experiment [40], the laboratory energies of the α beams are related to the ^{6}He energies by $E_{\alpha,\text{lab}} = \frac{3}{2} E_{^6\text{He,lab}}$ owing to the band pass of the solenoid ($B\rho = \sqrt{2mE_{\text{lab}}}/q$).

III. OPTICAL-MODEL ANALYSIS

The complex optical-model potential (OMP) is given by

$$U(r) = V_C(r) + V(r) + iW(r), \qquad (1)$$

where $V_C(r)$ is the Coulomb potential and $V(r)$ and $W(r)$ are the real and the imaginary parts of the nuclear potential, respectively. The real part of the potential is calculated from the folding procedure [41,42] using a density-dependent nucleon-nucleon interaction. The calculated folding potential is adjusted to the experimental scattering data by two parameters,

$$V(r) = \lambda V_F(r/w), \qquad (2)$$

where $\lambda \approx 1.1$–1.4 is the potential strength parameter [32] and $w \approx 1.0 \pm 0.05$ is the width parameter that slightly modifies the potential width. (Larger deviations of the width parameter w from unity would indicate a failure of the folding potential.) The nuclear densities of ^{120}Sn and α are
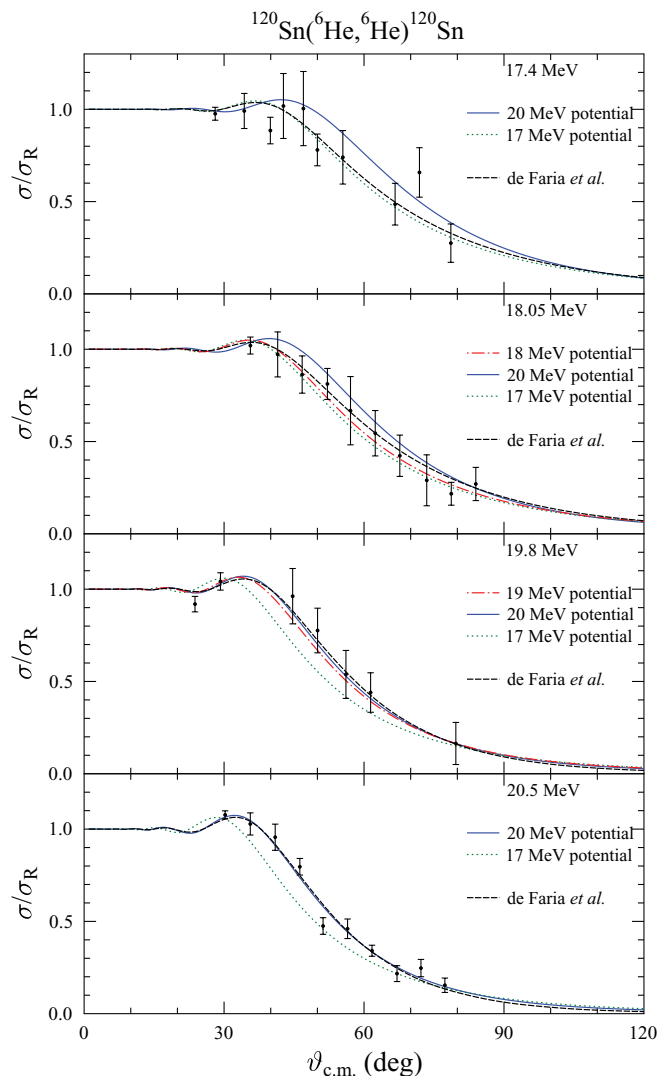

FIG. 1. (Color online) Rutherford-normalized elastic-scattering cross sections of ^{120}Sn(^{6}He,^{6}He)^{120}Sn reaction at $E_{\text{lab}} =$ 17.4, 18.05, 19.8, and 20.5 MeV versus the scattering angle $\vartheta_{\text{c.m.}}$ in the c.m. system (from Ref. [31]). The black dashed lines are the results from the original analysis in Ref. [31]. The blue solid lines are obtained from the fit to the 20-MeV data, and the green dotted lines are obtained from the fit to the 17-MeV data. The dash-dotted red lines are the interpolations for the 18- and 19-MeV data. The parameters of the fits are listed in Table I. For further discussion, see text (Sec. III A).

derived from the measured charge-density distributions that are compiled in Ref. [43]: For ^{120}Sn the three-parameter Gaussian distribution [44] is used. Almost identical folding potentials are obtained from the second available density distribution for ^{120}Sn [45], which has been measured in a smaller range of momentum transfers. For the α particle the sum-of-Gaussian parametrization of Ref. [46] is used. The ^{6}He density is taken from the ^{6}Li density determined in Ref. [47]; both nuclei ^{6}He and ^{6}Li have two nucleons in the p shell with similar separation energies. This density has been applied successfully in the calculation of ^{209}Bi(^{6}He,^{6}He)^{209}Bi elastic scattering [4,18]. Limitations of this choice may become visible in the width parameter w of the real part of the potential. However, a very
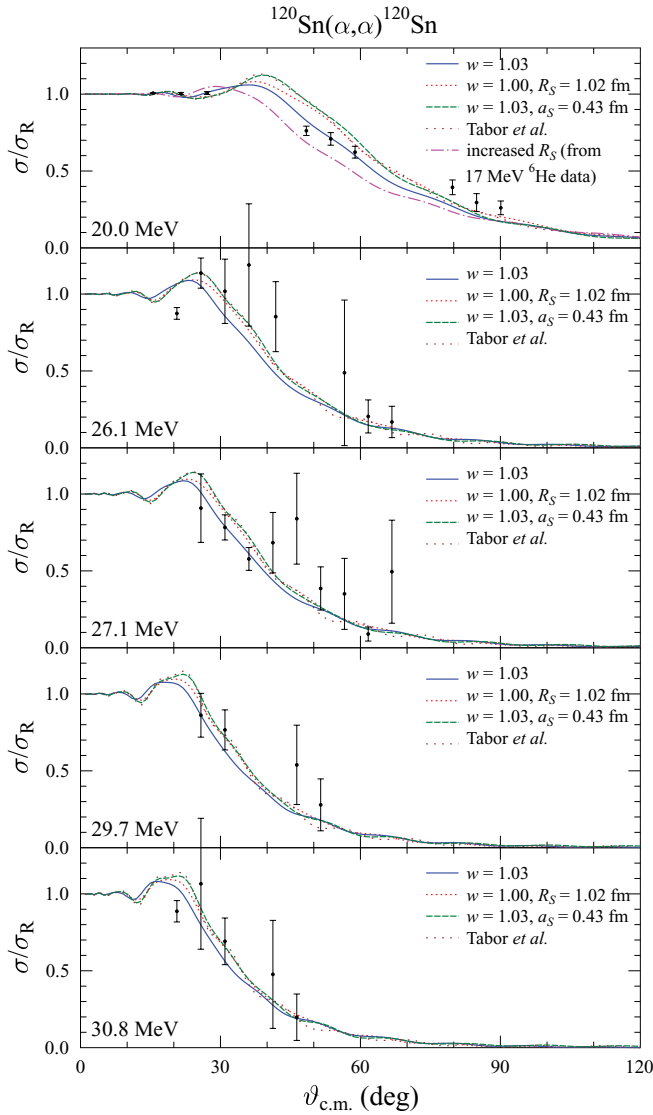
FIG. 2. (Color online) Rutherford-normalized elastic-scattering cross sections of the ^{120}Sn(α,α)^{120}Sn reaction at $E_{\rm lab} = 20.0, 26.1, 27.1, 29.7$, and 30.8 MeV versus the scattering angle $\vartheta_{\rm c.m.}$ in c.m. system. The lines are the results from the OM calculations in Sec. III B using different width parameters w of the real part and different imaginary radii R_S and diffusenesses a_S, as indicated in the figure. In addition, the influence of an increased imaginary radius R_S is shown for the 20-MeV data. The calculation of Tabor et al. [37] was adjusted to reproduce low-energy excitation functions (see Sec. III B3). For further details, see text (Sec. III B).

similar folding potential is obtained from recently published theoretical densities of ^{6}He [48]; the consequences of the different choices for the ^{6}He density will be studied in a subsequent article. For further details of the folding potential, see also Refs. [49,50].

The imaginary part $W(r)$ is taken in the usual Woods-Saxon parametrization. For the fits to the experimental data, we use volume and surface potentials,

$$W(r) = W_V \times f(x_V) + 4W_S \times \frac{df(x_S)}{dx_S}, \qquad (3)$$

with the potential depths W_V and W_S of the volume and surface parts, respectively, and

$$f(x_i) = \frac{1}{1 + \exp(x_i)} \qquad (4)$$

and $x_i = [r - R_i(A_P^{1/3} + A_T^{1/3})]/a_i$ with the radius parameters R_i in the heavy-ion convention, the diffuseness parameters a_i, and $i = S, V$. It is well established that at very low energies the surface contribution of the imaginary part is dominating; for example, in Ref. [51] it is suggested that the surface contribution is about 80% for α scattering of the neighboring nuclei ^{112}Sn and ^{124}Sn at energies below 20 MeV. At higher energies, that is, significantly above the Coulomb barrier, the volume contribution is dominating.

The Coulomb potential $V_C(r)$ is taken in the usual form of a homogeneously charged sphere. The Coulomb radius R_C is taken from the root-mean-square (rms) radius of the real folding potential with $w = 1.0$; the sensitivity of the calculations on minor changes of R_C is negligible.

For a fit to few data points of elastic scattering around the Coulomb barrier, the number of adjustable parameters should be as small as possible because there are significant ambiguities for the derived potentials; the underlying problem is that the elastic-scattering cross section is sensitive to the phase shifts and reflexion coefficients that are properties of the wave function far outside the nuclear radii: (i) the so-called "family problem" is a discrete ambiguity where real potentials with different depths lead to a similar description of the scattering data because the wave functions are very similar in the exterior, whereas in the interior the number of nodes may change. (ii) Continuous ambiguities are found: for example, a larger potential depth may be compensated by a smaller radius parameter, leading to more or less the same total potential strength and thus to the same wave function in the exterior region. In some cases this leads to a so-called "one-point potential" (e.g., Refs. [29,38,50,52]).

For a reduction of the adjustable parameters, we use the systematic behavior of the volume integrals of the potentials that has been found in Refs. [18,32]. For intermediate-mass and heavy nuclei, the volume integrals J_R of the real part of the potential are practically independent of the chosen nuclei and depend only weakly on energy with a maximum around 30 MeV. A Gaussian parametrization has been suggested in Ref. [53] for energies below and slightly above the maximum of J_R at $E_{R,0} = 30$ MeV:

$$J_R(E) = J_{R,0} \times \exp\left[-\frac{(E - E_{R,0})^2}{\Delta_R^2}\right], \qquad (5)$$

with the maximum value $J_{R,0} = 350$ MeV fm^3 and the width $\Delta_R = 75$ MeV. Potentials with J_R from Eq. (5) have been used for α scattering [32], α decay [53], and ^{6}He scattering [4,18]. The energy dependence of J_R is weak; for example, J_R changes by only a few percent in the considered energy range of this work. (Note that the negative signs of the volume integrals are, as usual, neglected in the discussion.)

Contrary to the real volume integrals J_R, the imaginary volume integrals J_I depend on the chosen nuclei and on energy. The energy dependence of J_I has been parametrized according

TABLE I. Parameters of the potentials of ^{120}Sn(^{6}He,^{6}He)^{120}Sn elastic scattering in Fig. 1.

E_{lab} (MeV)	λ	w[a]	J_R[b] (MeV fm^3)	r_R,rms (fm)	J_I[c] (MeV fm^3)	r_I,rms (fm)	W_S (MeV)	R_S (fm)	a_S[d] (fm)	σ_{reac} (mb)
17.40	1.207	0.95	339.0	5.477	75.6	9.320	19.2	1.315	0.7	1479
18.05	1.210	0.95	339.9	5.477	78.0	9.074	21.0	1.277	0.7	1503
19.80	1.219	0.95	342.4	5.477	83.8	8.415	26.6	1.174	0.7	1538
20.50	1.222	0.95	343.2	5.477	85.9	8.153	29.3	1.133	0.7	1546

[a]Fixed value, adjusted to the 20-MeV data.
[b]From Gaussian parametrization, Eq. (5).
[c]From Brown-Rho parametrization, Eq. (6).
[d]Fixed value.

to Brown and Rho [54],

$$J_I(E) = J_{I,0} \times \frac{(E - E_{I,0})^2}{(E - E_{I,0})^2 + \Delta_I^2}, \qquad (6)$$

with a saturation value $J_{I,0}$, the threshold value $E_{I,0} = 1.171$ MeV (corresponding to the first excited 2^+ state in ^{120}Sn), and the slope parameter Δ_I. Saturation values around $J_{I,0} \approx 100$ MeV fm^3 have been found in α scattering with a trend to smaller $J_{I,0}$ for doubly magic targets and increasing $J_{I,0}$ for semimagic or nonmagic targets. For the combination of a semimagic ^{6}He projectile and a semimagic ^{209}Bi target $J_{I,0} = 127$ MeV fm^3 and $\Delta_I = 12.7$ MeV were found [18]; these values are adopted for the analysis of ^{120}Sn(^{6}He,^{6}He)^{120}Sn elastic scattering, which is also a combination of a semimagic projectile and a semimagic target. For ^{120}Sn(α,α)^{120}Sn elastic scattering, a smaller saturation value of $J_{I,0} = 80$ MeV fm^3 is used, which is derived from scattering data at higher energies (see Sec. III B).

From the preceding considerations the volume integrals J_R and J_I for the analysis of ^{120}Sn(^{6}He,^{6}He)^{120}Sn and ^{120}Sn(α,α)^{120}Sn elastic scattering are fixed. Hence, the two adjustable parameters in the real part (strength parameter λ and width parameter w) are related by the volume integral J_R in Eq. (5), and the three adjustable Woods-Saxon parameters (depth W_V or W_S, radius R_V or R_S, and diffuseness a_V or a_S) are related by the volume integral J_I in Eq. (6).

A. ^{120}Sn(^{6}He,^{6}He)^{120}Sn

In addition to the preceding restrictions for the volume integrals J_R and J_I, we fix the imaginary surface diffuseness to a standard value $a_S = 0.7$ fm. The small volume part of the imaginary potential at low energies [51] is neglected: $W_V = 0$.

In a next step we adjust the remaining parameters to the ^{120}Sn(^{6}He,^{6}He)^{120}Sn scattering data at $E_{\mathrm{lab}} = 20.5$ MeV (referred to as "20-MeV data" in the following; the same convention of referring to the integer part of the laboratory energy E_{lab} is used for all data). An excellent description of the 20-MeV data is found (see Fig. 1, solid blue line) using a relatively small width parameter of $w = 0.95$ (see also Sec. III C). The same potential is now applied to the measured angular distributions at lower energies. Increasing discrepancies are observed for lower energies (Fig. 1, solid

blue lines): The calculated cross section at backward angles is larger than the measured values.

Because of the minor energy dependence of the real potential, the width parameter w was fixed now, and we tried to fit the lowest 17-MeV data by a readjustment of the imaginary part of the potential with a fixed J_I from Eq. (6). A clear increase of the radius parameter R_S by about 15% was found; then an excellent description of the 17-MeV data can be obtained. This 17-MeV potential is not able to describe the angular distributions at the other energies, where the calculated cross sections underestimate the experimental results at backward angles (Fig. 1, dotted green lines).

Finally, we interpolate the imaginary radius parameter R_S between the 17-MeV and the 20-MeV results and use it for the remaining 18- and 19-MeV angular distributions. An excellent agreement is obtained for all measured angular distributions (Fig. 1, dash-dotted red lines). The resulting parameters of the potentials are listed in Table I.

The total reaction cross sections σ_{reac} can be calculated from the reflexion coefficients η_L. We find that σ_{reac} decreases only slightly with energy from $\sigma_{\mathrm{reac}} = 1546$ mb at the highest energy $E_{\mathrm{lab}} = 20.5$ MeV to $\sigma_{\mathrm{reac}} = 1479$ mb at the lowest energy of $E_{\mathrm{lab}} = 17.4$ MeV (see Table I). These results agree with the original OM analysis of Ref. [31] within less than 5%.

For comparison, Fig. 1 shows also the original analysis of Ref. [31] using Woods-Saxon potentials without any restriction (black dashed lines). It is obvious that the systematic potentials from this work are able to reproduce the measured angular distributions with the same quality as the unrestricted Woods-Saxon potentials, which do not show any systematic bahavior; their volume integrals J_R and J_I vary strongly with energy.

B. ^{120}Sn(α,α)^{120}Sn

The analysis of the ^{120}Sn(α,α)^{120}Sn-system elastic scattering benefits from the fact that three angular distributions have been measured at higher energies [33–36]. These angular distributions can be used to fix the real part of the optical potential with small uncertainties. Thus, the number of adjustable parameters in the analysis of the new angular distributions at lower energies (see Fig. 2) is reduced, and the imaginary part can be deduced from the experimental data for a subsequent comparison with the ^{6}He case. Further information

on the potential can be obtained from the analysis of excitation functions that have been measured at lower energies [37,38].

Data at higher energies can be best reproduced using an imaginary potential of Woods-Saxon volume type. Somewhat arbitrarily, we take the three data sets from the literature at $E_{lab} = 34.4$ MeV [33], 40.0 MeV [34,35], and 50.5 MeV [36] as the "high-energy" data, which are analyzed with a volume Woods-Saxon imaginary part, whereas our new data below 30 MeV are analyzed as "low-energy" data using a surface Woods-Saxon imaginary part. Obviously, there must be an intermediate energy range with the transition from surface Woods-Saxon to volume Woods-Saxon potentials. This transitional region is around the 34-MeV data of Ref. [33]; however, these data are not adequate for a precise determination of the optical potential (see later in this article).

1. Angular distributions above ≈30 MeV

Three angular distributions of ^{120}Sn(α,α)^{120}Sn elastic scattering have been published. The data by Kuterbekov et al. [36] have been measured at $E_{lab} = 50.5$ MeV. The data cover an angular range from about $10°$ to $60°$. The numerical data are available in the EXFOR data base, but no further information on the experiment is available. The data of Baron et al. [34] are described in detail in an earlier report [35], including the numerical data with statistical errors. Because of very tiny statistical error bars in the forward direction of far below 1 %, a systematic error of 5% has been added quadratically to all data points. In addition, the given energy of $E_\alpha = 40.00 \pm 0.25$ MeV [35] has been reduced to an effective energy $E_{lab} = 39.95$ MeV because of the energy loss in the target. This angular distribution covers almost the full angular range from about $20°$ to $150°$. Finally, the data of Kumabe et al. [33] cover only a very limited angular range from about $20°$ to $60°$. The data have been extracted from Fig. 2 of Ref. [33], which shows the absolute cross sections without error bars. Because of the limited angular range, the uncertainties of the digitization procedure, and the missing error bars, any fit of these data has significant uncertainties.

The three angular distributions have been fitted using two adjustable parameters in the real part (strength parameter λ and width parameter w) and three parameters in the imaginary part (depth W_V, radius R_V, and diffuseness a_V). Additionally, the absolute values of the measured cross sections were allowed to vary. It is well known that the cross sections at forward directions practically do not depend on the underlying potentials; in particular, at very forward directions the cross section approaches the Rutherford cross section for all optical potentials. Thus, it is common practice to normalize the measured data to calculated values at forward directions because an absolute measurement requires the absolute determination of the target thickness and uniformity, detector solid angle, and beam current and a proper dead-time correction. The scaling factor s for the correction of the experimental data is defined by $\sigma_{exp}^{corr} = s \times \sigma_{exp}^{raw}$, where σ_{exp}^{raw} are the published cross-section data. It has been stated, for example, in Ref. [33], that this theoretical normalization s deviates by 10%–25% from unity for the tin targets used in that experiment. It is interesting to note that the obtained potential parameters are not very
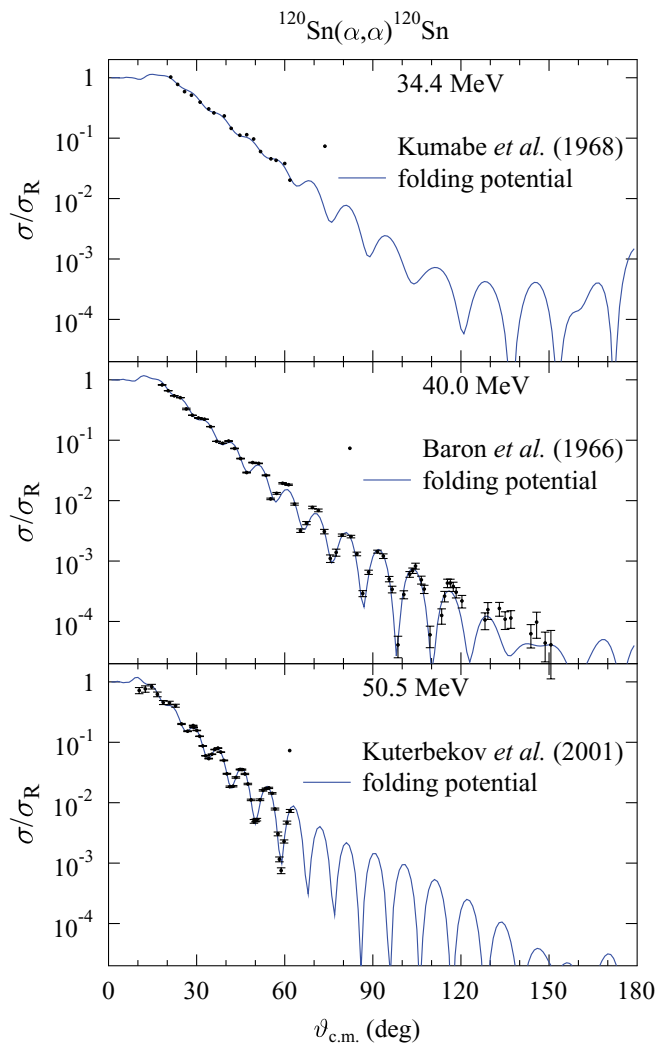

FIG. 3. (Color online) Rutherford-normalized elastic scattering cross sections of ^{120}Sn(α,α)^{120}Sn reaction at higher energies $E_{lab} =$ 34.4, 40.0, and 50.5 MeV [33–36] versus the scattering angle $\vartheta_{c.m.}$ in the c.m. frame. The calculated angular distributions use a double-folding potential in the real part and a volume Woods-Saxon potential in the imaginary part. For further details, see text.

sensitive to the scaling factor s as long as s remains far below a factor of two because the diffraction pattern in the experimental data at higher energies nicely defines the underlying potential.

The results of the analysis are shown in Fig. 3, and the obtained parameters are listed in Table II. Excellent agreement between the scaled experimental data and the theoretical analysis is found for all energies under study.

After a minor scaling of less than 20% ($s = 1.18$), the 50-MeV data can be described very well except for the two data points at most forward angles. Because of the reproduction of the diffraction pattern over the full measured angular range, it seems to be very unlikely that there is such a huge deviation between theory and experiment at small angles around $15°$. It should be kept in mind that the error bars in Ref. [36] are statistical only; however, because of the strong angular dependence of the Rutherford cross section, the uncertainties of data points at forward angles are usually defined by

TABLE II. Parameters of the potentials of ^{120}Sn(α,α)^{120}Sn elastic scattering at higher energies above 30 MeV in Fig. 3.

E_{lab} (MeV)	s	λ	w	J_R (MeV fm^3)	$r_{R,rms}$ (fm)	J_I (MeV fm^3)	$r_{I,rms}$ (fm)	W_V (MeV)	R_V (fm)	a_V (fm)	σ_{reac} (mb)
34.4	0.97	1.222	1.029	340.5	5.461	58.6	6.496	12.9	1.213	0.583	1742
40.0	1.48	1.190	1.048	347.4	5.561	77.2	6.495	16.7	1.173	0.543	1927
50.5	1.18	1.227	1.018	324.1	5.407	78.6	6.315	18.2	1.197	0.490	1939

systematic uncertainties (e.g., from the angular calibration or the dead-time correction).

The data of Baron *et al.* [34,35] cover almost the full angular range and are thus an ideal data set for the determination of the optical potential. The reproduction of the angular distribution is excellent over the full angular range. However, a significant scaling of the data ($s = 1.48$) was necessary; this seems to be justified because otherwise the most forward data point at 18° deviates by almost a factor of two from the Rutherford cross section.

As pointed out earlier, the data at 34 MeV [33] have less explanatory power. Here a small scaling factor of $s = 0.97$ is found. The reason for this $s \approx 1$ is simply that the authors of Ref. [33] have already applied the same normalization procedure to their data. The found deviation of 3% thus simply provides an estimate for the uncertainty of the digitization procedure that had to be used to extract the data from their Fig. 2.

From the obtained parameters (see Table II), the following conclusions can be drawn. The real part of the potential behaves very regularly with the expected decrease of the real volume integral J_R at higher energies [32]. The resulting J_R remains close to the suggested Gaussian parametrization in Eq. (5) although this parametrization is not expected to remain valid far above the maximum around 30 MeV [53]. The width parameter w is always slightly above 1.0; thus, for the following calculations at lower energies we adopt the average value of $\bar{w} = 1.032$. Together with the parametrization of J_R at low energies in Eq. (5), the real part of the optical potential is completely fixed now. The imaginary part increases with energy and saturates at $J_{I,0} \approx 80$ MeV fm^3. As expected, this value is somewhat smaller than the result for ^{6}He ($J_{I,0} = 127$ MeV fm^3). The available data are not sufficient to derive the slope parameter Δ_I of the Brown-Rho parametrization in Eq. (6). Instead, we use the same value $\Delta_I = 12.7$ MeV for α and ^{6}He in this article.

The relatively large value of $w = 1.032$ from the ^{120}Sn(α,α)^{120}Sn data at higher energies together with the small value of $w \approx 0.95$ derived from the ^{120}Sn(^{6}He,^{6}He)^{120}Sn data indicates that there is no major problem with the underlying ^{120}Sn density, which should show up as a modification for w in the same direction in both experiments. This is not surprising because the ^{120}Sn charge density has been measured in two independent experiments [44,45], and there is no evidence for a peculiar behavior of the neutron density (e.g., neutron skin) in ^{120}Sn [55,56]. Instead, it may be concluded that the chosen ^{6}He density is not very precise. Surprisingly, this problem was not found in the analysis of ^{209}Bi(^{6}He,^{6}He)^{209}Bi scattering data [4,18]; however, it may have been masked there by the larger Coulomb barrier of ^{209}Bi.

The largest width parameter $w = 1.048$ was obtained from the analysis of the 40-MeV angular distribution of Refs. [34,35]. A smaller width parameter of $w \approx 1.02$, closer to unity and in better agreement with the other data, can be obtained if the energy is changed to 42 MeV instead of 40 MeV. It is interesting to note that the authors of Refs. [34,35] later refer to their data as "42-MeV scattering data" [57], whereas in Ref. [35] it is explicitly stated that "the incident beam energy is 40.00 ± 0.25 MeV."

2. Angular distributions below ≈30 MeV

After fixing the complete real potential and the imaginary volume integral J_I as described in the previous section, now we fix the geometry of the imaginary part for the low-energy data below ≈30 MeV. Because of the dominating volume term at higher energies and the dominating surface term at lower energies (e.g., Ref. [51]), it is impossible to use at low energies the same geometry of the imaginary potential obtained at higher energies. Instead, we follow a procedure similar to the low-energy ^{6}He data. We fix the imaginary surface diffuseness at $a_S = 0.7$ fm, and we take the radius parameter R_S from the highest energy of the ^{120}Sn(^{6}He,^{6}He)^{120}Sn data: $R_S = 1.133$ fm. The depth of the potential W_S is adjusted to reproduce the volume integral J_I from Eq. (6) with the parameters $J_{I,0} = 80$ MeV fm^3 and $\Delta_I = 12.7$ MeV (as discussed in the previous subsection). As a consequence, all parameters of the potential are fixed, either to systematics or to the experimental data at higher energies. The reproduction of the ^{120}Sn(α,α) ^{120}Sn elastic scattering cross section is good for all energies (see Fig. 2). The parameters are listed in Table III. The total reaction cross section σ_{reac} shows the usual energy dependence; that is, it increases strongly with increasing energy.

In addition, we have studied the sensitivity of the data to minor variations of the potential. First, a width parameter $w = 1.0$ of the real potential was used instead of $w = 1.03$ together with a reduced imaginary radius parameter $R_S = 1.021$ fm (red dotted line in Fig. 2, adjusted to reproduce the excitation functions of Ref. [37]; see Sec. III B3). Second, the diffuseness a_S of the imaginary part was decreased to $a_S = 0.43$ fm instead of 0.7 fm (green dashed line, again adjusted to reproduce the excitations of Ref. [37]). In both cases the influence on the scattering cross sections remains relatively small although the 20-MeV data around 50° are clearly overestimated using $w = 1.0$ and $R_S = 1.021$ fm or $a_S = 0.43$ fm from the analysis of the excitation functions.

A significant reduction of the calculated scattering cross section is found if the increased radius parameter R_S from the 17-MeV ^{6}He data is taken at the lowest energy of the α data

TABLE III. Parameters of the potentials of ^{120}Sn(α,α)^{120}Sn elastic scattering in Figs. 2 and 4.

E_{lab} (MeV)	λ	w[a]	J_R[b] (MeV fm^3)	$r_{R,rms}$ (fm)	J_I[c] (MeV fm^3)	$r_{I,rms}$ (fm)	W_S (MeV)	R_S[d] (fm)	a_S[e] (fm)	σ_{reac} (mb)
20.0	1.207	1.032	343.0	5.474	53.8	7.910	13.1	1.133	0.70	1121
26.1	1.226	1.032	348.6	5.474	62.6	7.910	15.2	1.133	0.70	1663
27.1	1.228	1.032	349.1	5.474	63.6	7.910	15.5	1.133	0.70	1727
29.7	1.231	1.032	349.9	5.474	66.0	7.910	16.0	1.133	0.70	1870
30.8	1.231	1.032	350.0	5.474	66.9	7.910	16.2	1.133	0.70	1923
$\approx$13.5[f]	1.170	1.032	332.6	5.474	37.4	7.910	9.1	1.133	0.70	150
$\approx$13.5[f]	1.170	1.032	332.6	5.474	37.4	7.588	15.1	1.133	0.43[g]	86
$\approx$13.5[f]	1.284	1.000[g]	332.6	5.306	37.4	7.236	11.1	1.021[g]	0.70	61

[a]Fixed value from average of high-energy data.
[b]From Gaussian parametrization, Eq. (5).
[c]From Brown-Rho parametrization, Eq. (6).
[d]Fixed value from 20-MeV ^{6}He data.
[e]Fixed value.
[f]Average energy of excitation functions [37].
[g]Adjusted to excitation functions [37].

(magenta dash-dotted line). Here it becomes obvious that the new experimental ^{120}Sn(α,α)^{120}Sn data are not compatible with the strong increase of the radius parameter R_S at low energies that was essential for the reproduction of the ^{120}Sn(^{6}He,^{6}He)^{120}Sn data.

3. Excitation functions at low energies

Excitation functions have been measured by Tabor *et al.* and Badawy *et al.* [37,38]. Unfortunately, the latter article only mentions the measurement and derives a so-called one-point potential, but does not show the data for ^{120}Sn(α,α)^{120}Sn; thus, these data [38] are not accessible and cannot be used in the analysis. Tabor *et al.* [37] show two excitation functions at $\vartheta_{lab} = 120°$ and $165°$ in the energy range from 10 to 17 MeV in their Fig. 1. These data are shown together with the original analysis using a Woods-Saxon potential and the new reanalysis in Fig. 4.

In general, it is not possible to extract an optical potential from low-energy excitation functions because of ambiguities in the derived potentials. This has been clearly shown by Badawy *et al.* [38] in their analysis: "The only statement that can be made on the three parameters characterizing a Woods-Saxon real potential is that they are linked by the relation" that any potential with a depth of 0.2 MeV at $r = 10.63$ fm describes their experimental data. The imaginary potential also cannot be well determined: "... the results are very insensitive to the value of W...." Further details on the one-point potential and its relation to the so-called "family problem" of α-nucleus potentials are discussed in Ref. [50] using the precisely determined angular distribution of ^{144}Sm(α,α)^{144}Sm at $E \approx 20$ MeV (see Figs. 5 and 6 of Ref. [50]).

Although it is not possible to extract the optical potential, it is nevertheless possible to test the systematic potentials of this work using the measured excitation functions of Ref. [37]. It is found that the standard potential with $w = 1.03$, $R_S = 1.133$ fm, and $a_S = 0.7$ fm does not describe the excitation

functions at low energies (solid blue line in Fig. 4) and underestimates the measured cross sections. Instead of $a_S = 0.7$ fm, the diffuseness parameter of the surface imaginary part has to be decreased to $a_S = 0.43$ fm to find reasonable agreement with the measured excitation functions (green dashed line in Fig. 4). Alternatively, an excellent description of the data is also obtained using a reduced imaginary radius parameter $R_S = 1.021$ fm, $a_S = 0.7$ fm, and a width parameter $w = 1.0$ of the real part; however, such a width parameter w has been excluded by the high-energy angular distributions. This latter result is almost identical to the original analysis of Tabor *et al.* [37]; similar to that result, the angular distribution at 20 MeV is clearly overestimated around $50°$ (see Fig. 2).

Similar to the angular distributions shown in Fig. 2, a huge deviation from the measured excitation functions is found if the increased radius parameter $R_S = 1.315$ fm that has been obtained from the lowest energy in ^{120}Sn(^{6}He,^{6}He)^{120}Sn scattering is used (dash-dotted magenta lines in Figs. 2 and 4).

The calculated excitation functions may also change when the energy dependence of the volume integrals J_R and J_I in Eqs. (5) and (6) is varied. However, a variation of the Brown-Rho parameters of the order of 10% has only minor influence on the calculated excitation functions as long as the geometry of the imaginary potential is not changed.

The parameters of the potentials are also listed in Table III at the average energy $E_{lab} \approx 13.5$ MeV of the measured excitation functions [37]. At this energy both calculations with the slightly modified standard potential agree nicely with the measured data (see Fig. 4). However, the preferred calculation with $w = 1.03$ leads to slightly smaller elastic scattering cross sections, which have significant impact on the total reaction cross section σ_{reac}: $w = 1.03$ and $a_S = 0.43$ fm corresponds to $\sigma_{reac} = 86$ mb, $w = 1.0$ and $R_S = 1.021$ fm corresponds to $\sigma_{reac} = 61$ mb. The standard potential underestimates the elastic scattering cross sections of Ref. [37] and thus leads to a very high $\sigma_{reac} = 150$ mb. This discrepancy for σ_{reac} will affect the prediction of α-induced cross sections in the statistical model.

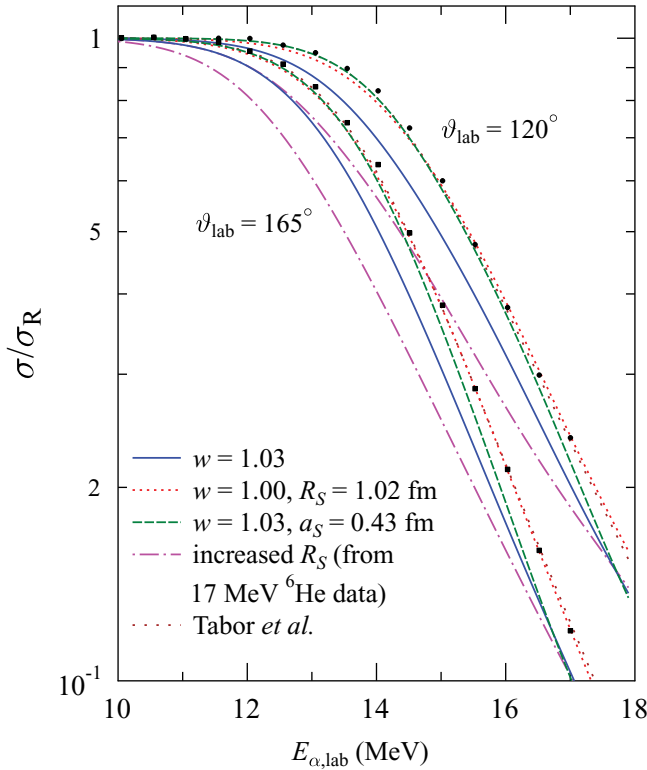FIG. 4. (Color online) Rutherford-normalized excitation function of ^{120}Sn(α,α)^{120}Sn elastic scattering at $\vartheta_{\text{lab}} = 120°$ and 165° [37]. An excellent description of the data at very low energies can be obtained using either a decreased imaginary diffuseness $a_S = 0.43$ fm (green dashed line) or a width parameter $w = 1.0$ and a reduced imaginary radius parameter R_S (red dotted line), whereas the standard potential slightly underestimates the measured data (solid blue line). For comparison, the original analysis of Tabor *et al.* [37] is also shown (brown short-dashed line, almost identical to the red dotted line). The increased imaginary radius from the low-energy ^{6}He data is clearly excluded (magenta dash-dotted line). For further discussion, see text.

C. Discussion

For a better understanding of the different behavior of the ^{120}Sn(α,α)^{120}Sn and ^{120}Sn(^{6}He,^{6}He)^{120}Sn scattering data we show in Figs. 5 and 6 the reflexion coefficients η_L that are related to the scattering matrix S_L by $S_L = \eta_L \times \exp(2i\delta_L)$; the reflexion coefficients η_L and the phase shifts δ_L are real. The shown η_L correspond to the S matrices from the calculations of Figs. 1 and 2. Both data sets show the usual behavior from η_L close to zero for small angular momenta L (corresponding to almost total absorption), increasing η_L for intermediate L (partial absorption), and $\eta_L \approx 1$ (no absorption) for large L. Again usual, with increasing energy the number of partly or totally absorbed partial waves increases. However, there are also significant differences in the shown η_L in Figs. 5 and 6.

The slope of the η_L vs L curves is different for the ^{6}He and the α data. Therefore, we plot the slope $d\eta_L/dL$ of this curve,

$$\frac{d\eta_L}{dL} := \frac{\eta_{L+1} - \eta_{L-1}}{(L+1) - (L-1)} = (\eta_{L+1} - \eta_{L-1})/2, \qquad (7)$$
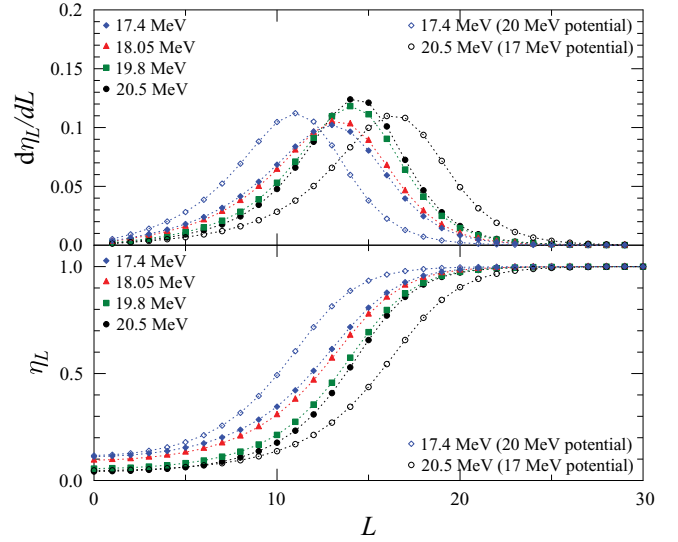

FIG. 5. (Color online) Reflexion coefficients η_L for ^{120}Sn(^{6}He,^{6}He)^{120}Sn elastic scattering at $E_{\text{lab}} = 17.4$, 18.05, 19.8, and 20.5 MeV (bottom) and the derivatives $d\eta_L/dL$ (top). The solid symbols correspond to the calculations in Fig. 1 and Table I; the open symbols are obtained using the 17-MeV potential at 20 MeV and vice versa. A clear broadening of the derivative $d\eta_L/dL$ at low energies can be seen. The data points for each L are connected by dotted lines to guide the eye. For further discussion, see text.

in the upper parts of Figs. 5 and 6. One finds curves with a shape close to Gaussian,

$$\frac{d\eta_L}{dL} \approx a \times \exp\left[-\frac{(L-L_0)^2}{(\Delta L)^2}\right], \qquad (8)$$

with the maximum slope at the angular momentum L_0 and the width ΔL. In general, the width ΔL is larger for the ^{6}He data than for the α data. In addition, a significant increase of the width ΔL toward lower energies is found for the ^{6}He data, which is not present in the α data. Significant absorption is found for all partial waves with $L \leqslant L_0 + \Delta L$.

For a better comparison of the ^{6}He data and the α data which have been measured at slightly different energies, we use the so-called reduced energy,

$$E_{\text{red}} = E \times \frac{A_P^{1/3} + A_T^{1/3}}{Z_P Z_T}, \qquad (9)$$

which takes into account the Coulomb barrier (which is the same for ^{6}He and α) and the different sizes of the ^{120}Sn-^{6}He and ^{120}Sn-α systems. The obtained values for the position L_0 of the maximum slope of η_L and the width ΔL are shown in dependence of the reduced energy E_{red} in Fig. 7.

It is obvious from Fig. 7 that the maximum slope of $d\eta_L/dL$ is found for larger L_0 in the ^{6}He case at the same reduced energy E_{red}, thus reflecting the larger mass and momentum and the larger absorption radius of the halo nucleus ^{6}He. More important, the width ΔL is larger for ^{6}He at the same E_{red} and increases significantly with decreasing energy. A similar effect is not seen for ^{120}Sn(α,α)^{120}Sn, and such a significant increase of the width ΔL is also not found in a series of high-precision α scattering data in this mass region on ^{89}Y, ^{92}Mo, ^{106,110,116}Cd,
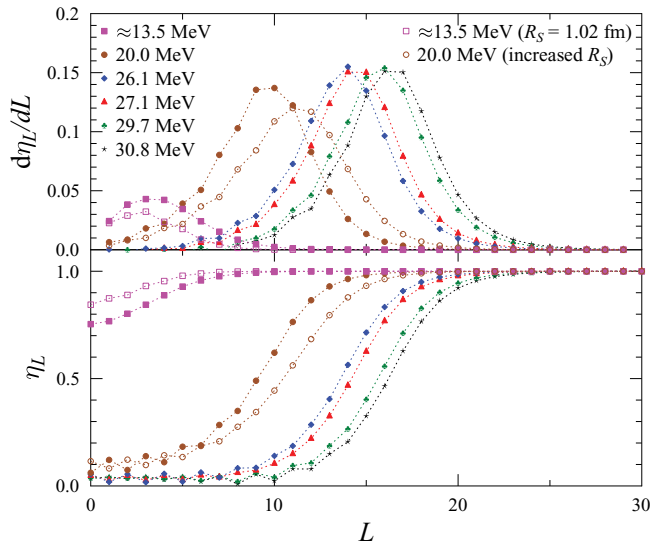
FIG. 6. (Color online) Reflexion coefficients η_L for ^{120}Sn(α,α)^{120}Sn elastic scattering at $E_{\text{lab}} = 20.0$, 26.1, 27.1, 29.7, and 30.8 MeV (bottom) and the derivatives $d\eta_L/dL$ (top). The solid symbols correspond to the calculations in Fig. 2 and Table III; the open symbols are obtained at the lowest energy of 20.0 MeV using an increased radius R_S of the imaginary surface potential (derived from ^{6}He scattering at the lowest energy). Additionally, the results from the excitation functions are shown at the average energy of $E_{\alpha,\text{lab}} = 13.5$ MeV using the standard potential with (solid squares) and the calculation with $w = 1.0$ and the reduced imaginary radius $R_S = 1.02$ fm (open squares). There is almost no broadening of the derivative $d\eta_L/dL$ at low energies, which is found only for ^{120}Sn(^{6}He,^{6}He)^{120}Sn (see Fig. 5). The data points for each L are connected by dotted lines to guide the eye. For further discussion, see text.

FIG. 7. (Color online) Position L_0 of the maximum derivative $d\eta_L/dL$ for ^{120}Sn(^{6}He,^{6}He)^{120}Sn and ^{120}Sn(α,α)^{120}Sn elastic scattering versus the reduced energy E_{red} in Eq. (9) (bottom) and the Gaussian width ΔL of $d\eta_L/dL$ in Eq. (8) (top). A clear broading of the width ΔL can only be seen for ^{120}Sn(^{6}He,^{6}He)^{120}Sn, whereas the width ΔL is almost constant for ^{120}Sn(α,α)^{120}Sn. The data for ^{120}Sn(α,α)^{120}Sn have been taken from the angular distributions in Fig. 2; the two points at the lowest energy result from the analysis of the excitation functions in Fig. 4 using either the standard potential or the potential with $w = 1.0$ and the reduced imaginary radius parameter $R_S = 1.02$ fm. The lines are to guide the eye. The open symbols show the result of the original analysis in Ref. [31].

and ^{112,124}Sn [51,58–60]. These interesting findings for ^{6}He are directly related to the energy dependence of the imaginary radius parameter R_S in the ^{6}He case.

For a demonstration of the strong influence of R_S in the ^{6}He case, we show in Fig. 5 the reflexion coefficients using the narrow imaginary potential from 20 MeV for the 17-MeV data and vice versa (open symbols); these calculations are in clear disagreement with the measured data, see Fig. 1. The narrow 20-MeV potential used at 17 MeV leads to a maximum of $d\eta_L/dL$ at lower L_0 and a smaller width ΔL. In parallel, σ_{reac} is reduced from 1479 mb to 1114 mb. The wide 17-MeV potential used at 20 MeV leads to an increased L_0, a larger width ΔL, and an increased $\sigma_{\text{reac}} = 1950$ mb instead of 1546 mb. In the α case, a similar result is found in the calculations where the increased radius parameter R_S at the lowest energy leads to an increased L_0, larger width ΔL, and an increased $\sigma_{\text{reac}} = 1459$ mb instead of 1121 mb. As can be seen from Fig. 2, the experimental data at 20 MeV are not reproduced using the larger radius parameter, and thus such an increase of L_0 and ΔL is excluded by the new ^{120}Sn(α,α)^{120}Sn scattering data. The description of the excitation functions at lower energies requires either a reduced diffuseness $a_S = 0.43$ fm or a reduced radius $R_S = 1.021$ fm in combination with $w = 1.0$ but does clearly not require any increased
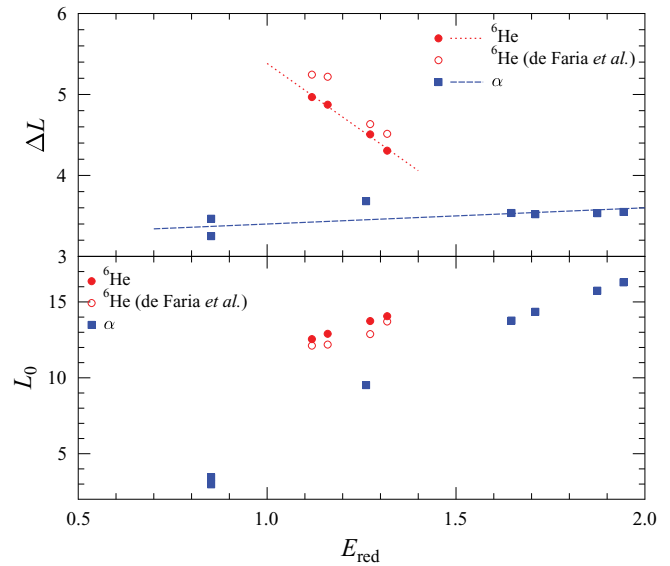
imaginary radius as derived from the low-energy ^{6}He data. Again, this clearly excludes any increase in L_0 or ΔL in the α case (see Fig. 7).

In summary, we find the following properties of the ^{120}Sn-α potential. The high-energy data define the width parameter $w = 1.03$ for the folding potential in the real part. The volume integrals J_R and J_I of the real and imaginary potentials are consistent with several systematic studies. The geometry of the imaginary part is of Woods-Saxon volume type at higher energies; here the parameters can be fitted to the measured angular distributions. At lower energies the surface contribution is dominating. The imaginary diffuseness is fixed here at a standard value $a_S = 0.7$ fm. The reduced radius parameter R_S is constant above 20 MeV and identical to the analysis of ^{120}Sn(^{6}He,^{6}He)^{120}Sn scattering at the highest measured energy. Only at very low energies does a_S have to be reduced or $w = 1.0$ and a reduced imaginary radius $R_S = 1.02$ fm have to be used. In any case, there is no significant broadening of the $d\eta_L/dL$ vs L curve; a significant broadening of $d\eta_L/dL$ is only seen for the ^{6}He case.

We have repeated the preceding analysis of the slope $d\eta_L/dL$ with the original Woods-Saxon potentials which were fitted to the experimental ^{120}Sn(^{6}He,^{6}He)^{120}Sn data [31]. The same general behavior of L_0 and ΔL is found from this analysis (see open symbols in Fig. 7). Thus, it can be concluded that the experimental ^{120}Sn(^{6}He,^{6}He)^{120}Sn data clearly require a larger value L_0 and an increasing width ΔL at

lower energies. This finding is independent whether systematic folding potentials or fitted Woods-Saxon potentials are applied in the analysis. Consequently, this increase of the width ΔL in the $d\eta_L/dL$ vs L curve may be taken as a signature for the halo properties of the ^{6}He projectile. Whereas ΔL changes by about $+0.2$ for E_{red} between 0.85 and 1.85 MeV in the α case, a one-order-of-magnitude-stronger variation of about -0.6 within a much smaller range of 1.1 MeV $\leqslant E_{\mathrm{red}} \leqslant$ 1.3 MeV is found for the ^{6}He case:

$$\frac{\Delta(\Delta L)}{\Delta E_{\mathrm{red}}} \approx +0.2/\mathrm{MeV} \quad \text{for } \alpha, \tag{10}$$

$$\frac{\Delta(\Delta L)}{\Delta E_{\mathrm{red}}} \approx -3.0/\mathrm{MeV} \quad \text{for } ^6\mathrm{He}. \tag{11}$$

Halo properties may be assigned as soon as the variation of ΔL with E_{red} is clearly below a value of $\Delta(\Delta L)/\Delta E_{\mathrm{red}} \approx -1/$ MeV around $E_{\mathrm{red}} \approx 1$ MeV.

The increase of the imaginary radius parameter R_S has been explained in Ref. [18] with the fact that the area where reactions may occur moves to larger distances at lower energies. This has been clearly shown, for example, for low-energy capture data in the ^{16}O(p,γ)^{17}F reaction [61–63]. Further work is required to follow this idea in more detail.

The systematic behavior of the potentials in the real and imaginary parts may be used as the basis for the construction of a simple global ^{6}He potential. Because of the smooth variation of all parameters, the predictive power of such a global ^{6}He potential should be very good. In particular, it has to be pointed out that the so-called "threshold anomaly" is avoided in the present study. Such "threshold anomalies," that is, potentials with a strong or unusual energy dependence at energies around the Coulomb barrier, or with unusual geometry parameters such as a huge imaginary diffuseness a_S of several fm, had to be used in many studies to reproduce the huge total reaction cross sections of halo nuclei around the barrier (e.g., Refs. [3,31]). For a deeper discussion of threshold anomalies and dynamic polarization potentials, see, for example, Refs. [64–67].

For completeness, it has also to be pointed out that an unusually large reaction cross section is not already a clear signature of a halo wave function. Such an unusual σ_{reac} only indicates the strong coupling to other channels which may not at all be related to halo properties. For example, such a behavior has been found in the elastic scattering of ^{18}O by ^{184}W where the coupling to the low-lying 2^+ state of ^{184}W leads to an unusual elastic scattering angular distribution and a huge σ_{reac} [68–70].

IV. SUMMARY AND CONCLUSIONS

We have presented new experimental data for ^{120}Sn(α,α)^{120}Sn elastic scattering at energies around and slightly above the Coulomb barrier which were measured simultaneously with a recent ^{120}Sn(^{6}He,^{6}He)^{120}Sn experiment. The data are successfully analyzed using systematic folding potentials in the real part and smoothly varying Woods-Saxon potentials in the imaginary part. These potentials are also able to reproduce ^{120}Sn(α,α)^{120}Sn angular distributions at higher energies and excitation functions at lower energies that are available in literature. A comparison with the ^{120}Sn(^{6}He,^{6}He)^{120}Sn scattering data shows that similar potentials with a smooth mass and energy dependence are also able to reproduce these data. Thus, this smoothly varying potential may be used as the basis for the construction of simple global ^{6}He potential with expected good predictive power.

The halo properties of ^{6}He lead to an enhanced total reaction cross section at low energies that is related to a relatively small elastic scattering cross section at intermediate and backward angles. This behavior requires—as the only special feature for the ^{6}He case—an energy-dependent radius parameter R_S that increases toward lower energies. Such an increase of the radius parameter R_S is not seen in the new ^{120}Sn(α,α)^{120}Sn data and was also not found in a series of high-precision α scattering of neighboring target nuclei around 20 MeV. At very low energies even an opposite trend is seen in the analysis of the excitation functions of Ref. [37].

The increase of the radius parameter R_S of the ^{6}He potential toward lower energies is related to a relatively smooth rise of the reflexion coefficients η_L as a function of angular momentum L. In particular, it is found that the width ΔL of the almost Gaussian-shaped slope $d\eta_L/dL$ is significantly larger for ^{6}He than for α. The width ΔL shows an increase toward lower energies for ^{6}He that is not present in the α-scattering data. This characteristic behavior of the ^{6}He data can be used as a signature for the halo properties of ^{6}He, and it should be tested as a general signature of halo properties in elastic scattering in other cases, such as ^{11}Be. We suggest a value below $\Delta(\Delta L)/\Delta E_{\mathrm{red}} \approx -1/$ MeV at $E_{\mathrm{red}} \approx 1$ MeV as signature for halo properties. Although the quality of the presented new ^{120}Sn(α,α)^{120}Sn scattering data is clearly inferior to recent high-precision data in this mass region, only the combined analysis of the new data for ^{120}Sn(α,α)^{120}Sn scattering together with angular distributions at higher energies and excitation functions at lower energies enables the comparison between ^{120}Sn(α,α)^{120}Sn and ^{120}Sn(^{6}He,^{6}He)^{120}Sn elastic scattering and the derivation of the preceding new results.

[1] R. E. Warner *et al.*, Phys. Rev. C **51**, 178 (1995).

[2] J. J. Kolata *et al.*, Phys. Rev. Lett. **81**, 4580 (1998).

[3] E. F. Aguilera *et al.*, Phys. Rev. Lett. **84**, 5058 (2000).

[4] E. F. Aguilera *et al.*, Phys. Rev. C **63**, 061603 (2001).

[5] O. R. Kakuee *et al.*, Nucl. Phys. A **728**, 339 (2003).

[6] O. R. Kakuee *et al.*, Nucl. Phys. A **765**, 294 (2006).

[7] A. M. Sánchez-Benítez *et al.*, Nucl. Phys. A **803**, 30 (2008).

[8] A. Navin *et al.*, Phys. Rev. C **70**, 044601 (2004).

[9] A. Di Pietro *et al.*, Phys. Rev. C **69**, 044613 (2004).

[10] A. Chatterjee *et al.*, Phys. Rev. Lett. **101**, 032701 (2008).

[11] M. Milin *et al.*, Nucl. Phys. A **730**, 285 (2004).

[12] N. Keeley, K. W. Kemper, O. Momotyuk, and K. Rusek, Phys. Rev. C **77**, 057601 (2008).

[13] M. Mazzocco *et al.*, Eur. Phys. J. A **28**, 295 (2006).

[14] M. Mazzocco *et al.*, Eur. Phys. J. Spec. Top. **150**, 37 (2007).

[15] A. Di Pietro *et al.*, Phys. Rev. Lett. **105**, 022701 (2010).

[16] N. Keeley, R. Raabe, N. Alamanos, and J. L. Sida, Prog. Part. Nucl. Phys. **59**, 579 (2007).

[17] N. Keeley, N. Alamanos, K. W. Kemper, and K. Rusek, Prog. Part. Nucl. Phys. **63**, 396 (2009).

[18] P. Mohr, Phys. Rev. C **62**, 061601(R) (2000).

[19] K. Rusek, N. Keeley, K. W. Kemper, and R. Raabe, Phys. Rev. C **67**, 041604(R) (2003).

[20] N. Keeley, J. M. Cook, K. W. Kemper, B. T. Roeder, W. D. Weintraub, F. Marechál, and K. Rusek, Phys. Rev. C **68**, 054601 (2003).

[21] B. Abu Ibrahim and Y. Suzuki, Phys. Rev. C **70**, 011603(R) (2004).

[22] K. Rusek, I. Martel, J. Gómez-Camacho, A. M. Moro, and R. Raabe, Phys. Rev. C **72**, 037603 (2005).

[23] A. M. Moro, K. Rusek, J. M. Arias, J. Gómez-Camacho, and M. Rodríguez-Gallardo, Phys. Rev. C **75**, 064607 (2007).

[24] L. Borowska, K. Terenetsky, V. Verbitsky, and S. Fritzsche, Phys. Rev. C **76**, 034606 (2007).

[25] N. Keeley and N. Alamanos, Phys. Rev. C **77**, 054602 (2008).

[26] R. S. Mackintosh and N. Keeley, Phys. Rev. C **79**, 014611 (2009).

[27] Y. Kucuk, I. Boztosun, and N. Keeley, Phys. Rev. C **79**, 067601 (2009).

[28] S. N. Ershov, L. V. Grigorenko, J. S. Vaagen, and M. V. Zhukov, J. Phys. G **37**, 064026 (2010).

[29] J. P. Fernández-García, M. Rodríguez-Gallardo, M. A. G. Alvarez, and A. M. Moro, Nucl. Phys. A **840**, 19 (2010).

[30] V. K. Lukyanov, D. N. Kadrev, E. V. Zemlyanaya, A. N. Antonov, K. V. Lukyanov, and M. K. Gaidarov, Phys. Rev. C **82**, 024604 (2010).

[31] P. N. de Faria *et al.*, Phys. Rev. C **81**, 044605 (2010).

[32] U. Atzrott, P. Mohr, H. Abele, C. Hillenmayer, and G. Staudt, Phys. Rev. C **53**, 1336 (1996).

[33] I. Kumabe, H. Ogata, T.-H. Kim, M. Inoue, Y. Okuma, and M. Matoba, J. Phys. Soc. Jpn. **25**, 14 (1968).

[34] N. Baron, R. F. Leonard, J. L. Need, W. M. Stewart, and V. A. Madsen, Phys. Rev. **146**, 861 (1966).

[35] N. Baron, R. F. Leonard, J. L. Need, and W. M. Stewart, NASA Report TN D-3067, 1967 (unpublished).

[36] K. A. Kuterbekov, A. Dujsebaev, B. M. Sadykov, and A. M. Mukhamedjanova, *51 Workshop on Nuclear Spectroscopy and Nuclear Structure* (Sarov, Russia, 2001), p. 194.

[37] S. L. Tabor, B. A. Watson, and S. S. Hanna, Phys. Rev. C **11**, 198 (1975).

[38] I. Badawy, B. Berthier, P. Charles, M. Dost, B. Fernandez, J. Gastebois, and S. M. Lee, Phys. Rev. C **17**, 978 (1978).

[39] R. Lichtenthäler *et al.*, Eur. Phys. J. A **25**, 733 (2005).

[40] P. N. de Faria, Ph.D. thesis, Institute of Physics of the University of São Paulo, IFUSP, 2008.

[41] A. M. Kobos, B. A. Brown, R. Lindsay, and G. R. Satchler, Nucl. Phys. A **425**, 205 (1984).

[42] G. R. Satchler and W. G. Love, Phys. Rep. **55**, 183 (1979).

[43] H. de Vries, C. W. de Jager, and C. de Vries, At. Data Nucl. Data Tables **36**, 495 (1987).

[44] J. R. Ficenec, L. A. Fajardo, W. P. Trower, and I. Sick, Phys. Lett. B **42**, 213 (1972).

[45] P. Barreau and J. B. Bellicard, Phys. Lett. B **25**, 470 (1967).

[46] I. Sick, Phys. Lett. B **116**, 212 (1982).

[47] G. C. Li, I. Sick, R. R. Whitney, and M. R. Yearian, Nucl. Phys. A **162**, 583 (1971).

[48] I. Brida and F. M. Nunes, Nucl. Phys. A **847**, 1 (2010).

[49] H. Abele and G. Staudt, Phys. Rev. C **47**, 742 (1993).

[50] P. Mohr, T. Rauscher, H. Oberhummer, Z. Máté, Zs. Fülöp, E. Somorjai, M. Jaeger, and G. Staudt, Phys. Rev. C **55**, 1523 (1997).

[51] D. Galaviz, Zs. Fülöp, Gy. Gyürky, Z. Máté, P. Mohr, T. Rauscher, E. Somorjai, and A. Zilges, Phys. Rev. C **71**, 065802 (2005).

[52] C. Signorini *et al.*, Phys. Rev. C **61**, 061603(R) (2000).

[53] P. Mohr, Phys. Rev. C **61**, 045802 (2000).

[54] G. E. Brown and M. Rho, Nucl. Phys. A **372**, 397 (1981).

[55] M. Warda, X. Viñas, X. Roca-Maza, and M. Centelles, Phys. Rev. C **81**, 054309 (2010).

[56] B. Özel, J. Enders, H. Lenske, P. von Neumann-Cosel, I. Poltoratska, V. Yu. Ponomarev, A. Richter, D. Savran, and N. Tsoneva, arXiv:0901.2443.

[57] N. Baron, R. F. Leonard, and W. M. Stewart, Phys. Rev. C **4**, 1159 (1971).

[58] G. G. Kiss *et al.*, Phys. Rev. C **80**, 045807 (2009).

[59] Zs. Fülöp *et al.*, Phys. Rev. C **64**, 065805 (2001).

[60] G. G. Kiss, Zs. Fülöp, Gy. Gyürky, Z. Máté, E. Somorjai, D. Galaviz, A. Kretschmer, K. Sonnabend, A. Zilges, Eur. Phys. J. A **27** (Suppl. 1), 197 (2006), and to be published.

[61] H. C. Chow, G. M. Griffiths, and T. H. Hall, Can. J. Phys. **53**, 1672 (1975).

[62] R. Morlock, R. Kunz, A. Mayer, M. Jaeger, A. Müller, J. W. Hammer, P. Mohr, H. Oberhummer, G. Staudt, and V. Kölle, Phys. Rev. Lett. **79**, 3837 (1997).

[63] C. Iliadis, C. Angulo, P. Descouvemont, M. Lugaro, and P. Mohr, Phys. Rev. C **77**, 045802 (2008).

[64] C. Mahaux, H. Ngô, and G. R. Satchler, Nucl. Phys. A **449**, 354 (1986).

[65] I. J. Thompson, M. A. Nagarajan, J. S. Lilley, and M. J. Smithson, Nucl. Phys. A **505**, 84 (1989).

[66] S. Kailas and P. Singh, Phys. Rev. C **50**, 1230 (1994).

[67] J. O. Fernández Niello *et al.*, Nucl. Phys. A **787**, 484 (2007).

[68] C. E. Thorn, M. J. LeVine, J. J. Kolata, C. Flaum, P. D. Bond, and J.-C. Sens, Phys. Rev. Lett. **38**, 384 (1977).

[69] W. G. Love, T. Terasawa, and G. R. Satchler, Nucl. Phys. A **291**, 183 (1977).

[70] G. R. Satchler, Phys. Rep. **199**, 147 (1991).